Disentangling contributions from iron and myelin architecture to brain tissue magnetic susceptibility by using Quantitative Susceptibility Mapping (QSM)

Ferdinand Schweser[1], Andreas Deistung[1], Karsten Sommer[1], and Jürgen Rainer Reichenbach[1]
[1]*Medical Physics Group, Dept. of Diagnostic and Interventional Radiology I, Jena University Hospital, Jena, Germany*

INTRODUCTION – Magnetic susceptibility is an intrinsic physical tissue property which recently became accessible *in vivo* by a novel imaging technique called quantitative susceptibility mapping (QSM) [1,2]. Susceptibility maps of the human brain demonstrate astounding anatomical contrast [1,2], which is currently believed to be predominantly due to iron (paramagnetic) and myelin-lipids (diamagnetic) [3]. The intermixing of both contributions, however, complicates interpretation of susceptibility changes in particular in neurodegenerative diseases where inflammatory myelin-loss and focal iron accumulation may occur simultaneously. It has, furthermore, recently been discovered that a considerable orientation dependence of brain tissue susceptibility exists, which further complicates interpretation. We present a novel technique for substantially increasing the specificity of QSM by utilizing additional R_2* information. The technique yields two novel contrasts, one that is independent of orientation effects, whereas the other is independent of tissue iron concentration.

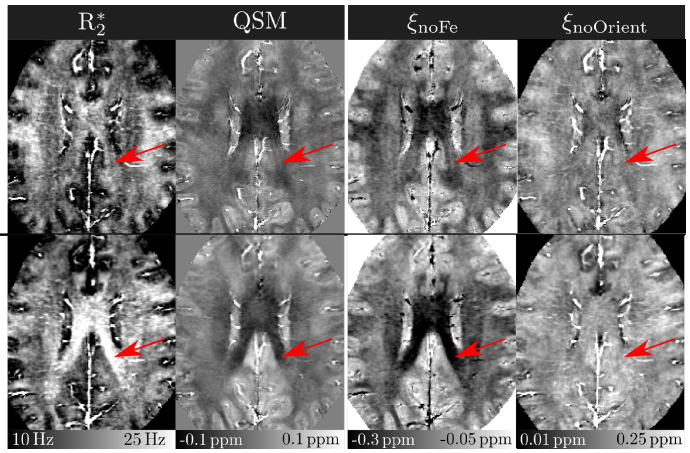

FIGURE 1. Input data (R_2*, QSM) and novel contrasts (ξ_{noFe}, $\xi_{noOrient}$) with the volunteer's head in two different orientations (top and bottom). The arrows point to considerable orientation dependent contrast in the input datasets.

THEORY – A three compartment tissue model was assumed with punctuate particle inclusions (called iron in the following) and myelinated axons in a homogenous tissue matrix. In this model, the bulk voxel susceptibility can be expressed by **Eq. 1** (volume fraction of iron neglected) [1]. The corresponding relation for the effective transverse relaxation rate, R_2*, is given by **Eq. 2** [4,5]. In both equations the terms associated with myelin depend on the orientation of the axons relative to the main magnetic field (angle ϑ) as described by **Eq. 3** [5] and **Eq. 4** [6,7]. The dependence on iron concentration may be eliminated from the equations by linear combination of Eq. 1 and Eq. 2 according to **Eq. 5**, yielding a novel iron-independent contrast ξ_{noFe}. The coefficient $\hat{\chi}_{Fe}\hat{r}_{Fe}^{-1}$ may be estimated from literature values (this study; see Tab. 2) or from R_2* and susceptibility values in regions with a similar contribution of myelin. The contrast ξ_{noFe} depends linearly on the myelin-lipid volume fraction and includes the myelin-related orientation dependencies. A rotation invariant contrast may be generated by a linear combination of Eqs. 1 and 2 that eliminates the ϑ-terms according to **Eq. 6**. This contrast is linear with respect to both the iron concentration and the myelin volume fraction.

MATERIALS AND METHODS – To demonstrate the technique, high-resolution double-echo GRE data was acquired from the brain of a volunteer (male, 26y) using the ToF-SWI-sequence [9] (TE_1/TE_2=3.38ms/22ms, TR=30ms, FA=20°, 600µm isotropic voxels; acquisition time: 15min.) on a 3 Tesla whole-body MRI scanner (Tim Trio, Siemens Medical Solutions, Erlangen, Germany) using a 12-channel receive head-matrix coil. The scan was repeated with the volunteer's head in head-to-neck position to investigate orientation effects. The resulting complex-valued images were registered to the normal head position using FSL-FLIRT (FMRIB, Oxford University). R_2* maps were computed from the magnitude echoes with compensation of Rician noise [10] and susceptibility maps were reconstructed from the phase images using the HEIDI algorithm [submitted to ISMRM]. The maps were, finally, combined according to Eqs. 5 and 6. The unknown constant $\chi^{\perp-\parallel}\cdot\hat{r}_{My}^{-1}$ in Eq. 6 was determined by minimizing the difference between the orientation independent contrasts, $\xi_{noOrient}$, of the two head orientations (A,B) in the corpus callosum: $\min\left\|\xi_{noOrient}^{A}-\xi_{noOrient}^{B}\right\|_2^2$.

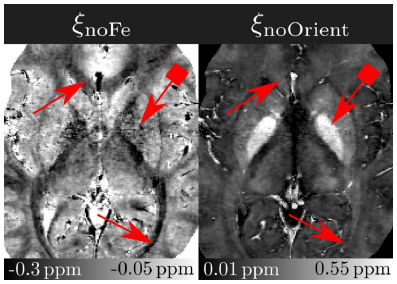

FIGURE 2. Novel contrast in the iron-laden basal ganglia region (normal head position). Straight arrows mark orientation dependent myelin contrast (left only). Square-ended arrows mark contrast due to iron (right only).

RESULTS – The experimentally determined value of $\chi^{\perp-\parallel}\cdot\hat{r}_{My}^{-1}$ was (7.9 ± 0.4) ppm/Hz. Figure 1 depicts R_2* maps and susceptibility maps as well as the two new contrasts. The R_2* and susceptibility maps of the two head orientations demonstrate substantial different contrast in the region of the corpus callosum (arrows) due to anisotropic magnetic properties of myelin (Eqs. 3 and 4). This orientation dependence is also present in the new iron-independent contrast, ξ_{noFe}, which, furthermore, delineates cortical gray matter supporting recent results that attribute the susceptibility contrast between cortex and white matter to different myelin content [1,3]. The orientation independent contrast, $\xi_{noOrient}$, was relatively homogeneous compared to the other contrasts and demonstrated only minor intensity variations between the two head orientations which may be attributed to inaccurate QSM or R_2* reconstruction. Figure 2 shows slices of the basal ganglia region. Iron laden nuclei were discernable only in the $\xi_{noOrient}$ images (square-ended arrows) while major fiber tracts were delineated predominantly in the ξ_{noFe} images (straight arrows).

DISCUSSION AND CONCLUSIONS – The proposed technique disentangles magnetic properties related to punctuate susceptibility inclusions and myelin architecture using magnitude and phase signal of a clinically established GRE sequence. The coefficient $\hat{\chi}_{Fe}\hat{r}_{Fe}^{-1}$ in Eq. 5 is independent of the magnetic moment of the particles [11]. Variations in the iron-independent contrast, ξ_{noFe}, therefore, cannot be attributed to any type of punctuate paramagnetic inclusions, such as ferritin cores or transferrin molecules. The technique, thus, provides a unique means for specifically investigating the contentious biophysical source of pathological tissue susceptibility variations *in vivo*, e.g., in white-matter lesions of multiple sclerosis patients. The orientation-independent contrast, $\xi_{noOrient}$, represents a mixture of contributions from iron and myelin. It may, however, be supposed that $\xi_{noOrient}$ is relatively insensitive to variations of myelin content, because the value of $\chi^{\parallel}$ has recently been shown to be similar to the matrix susceptibility [6]. Future studies will involve *post mortem* experiments for thoroughly investigating the specificity and sensitivity of the proposed technique.

Tissue model:

(1) $\chi = c_{Fe}\hat{\chi}_{Fe} + v_{My}\chi_{My} + (1-v_{My})\cdot\chi_m$

(2) $R_2^* = c_{Fe}\hat{r}_{Fe} + v_{My}d_{MyAx}r_{MyAx} + R_0^*$

Myelin contributions:

(3) $r_{MyAx} = \hat{r}_{MyAx}\sin^2\vartheta$

(4) $\chi_{My} = \chi^{\parallel} + \chi^{\perp-\parallel}\cdot\sin^2\vartheta,\quad \chi^{\perp-\parallel} \equiv \chi^{\perp} - \chi^{\parallel}$

New contrasts:

(5) $\xi_{noFe} = \Delta\chi - \hat{\chi}_{Fe}\hat{r}_{Fe}^{-1}\cdot R_2^*$
$= v_{My}\cdot(\chi_{My} - \chi_m - d_{MyAx}\hat{\chi}_{Fe}\hat{r}_{Fe}^{-1}r_{MyAx}) + \xi_{m,1}$

(6) $\xi_{noOrient} = \Delta\chi - \chi^{\perp-\parallel}\cdot\hat{r}_{My}^{-1}\cdot R_2^*$
$= c_{Fe}\cdot(\hat{\chi}_{Fe} - \chi^{\perp-\parallel}\cdot\hat{r}_{My}^{-1}\hat{r}_{Fe}) + \ldots$
$\ldots + v_{My}\cdot(\chi^{\parallel} - \chi_m) + \xi_{m,2}$

TABLE 1. Equations referenced in the text. Variables are explained in Table 2.

REFERENCES – [1] Schweser F et al., 2011. *NeuroImage*. 54:2789-807. [2] Schäfer A et al., 2011. *Hum Brain Mapp*. [3] Langkammer C et al., 2011. *NeuroImage*. [4] Yao B et al., 2009. *NeuroImage*. 44:1259-66. [5] Bender B and Klose U, 2010. NMR Biomed. 23:1071-6. [6] Li W et al., 2011. *NeuroImage*. [7] Lee J et al., 2011. *NeuroImage*. 57:225-34. [8] Schenck JF, 1992. *Ann N Y Acad Sci*. 649:285-301. [9] Deistung A et al., 2009. *J Magn Reson Imaging*. 29:1478-1484. [10] Miller AJ and Joseph PM, 1993. *Magn Reson Imaging*. 11:1051-6. [11] Yablonskiy DA and Haacke EM, 1994. *Magn Reson Med*. 32:749-63.

c_{Fe}	concentration of iron
v_{My}	voxel volume fraction of myelin-lipids
$\hat{\chi}_{Fe}$	molar susceptibility of iron (1.27 ppm per kg iron/kg wet mass [8])
χ_{My}	susceptibility of myelin-lipids
χ_m	susceptibility of tissue matrix
$\chi^{\parallel}, \chi^{\perp}$	susceptibility of myelin sheath parallel and perpendicular to the magnetic field, resp.
$\hat{r}_{Fe}$	relaxivity of iron (144 Hz per kg iron/kg tissue wet mass at 3T [4])
r_{MyAx}	relaxation rate due to myelinated axons
d_{MyAx}	volume fraction of myelin-lipids relative to the volume of a myelinated axon
R_0^*	all effects not due to iron and myelin
$\xi_{m,1/2}$	matrix contributions to ξ_{noFe} and $\xi_{noOrient}$

TABLE 2. Explanation of variables.